

**RESEARCH ARTICLE**

# Triaxial Analysis of Mechanical Properties in Additively Manufactured Layered Material

Ghoulem Ifrene<sup>1</sup>  | Richard Schultz<sup>1</sup> | Prasad Pothana<sup>1</sup> | Neal Nage<sup>2</sup> | Kuldeep Singh<sup>3</sup>  | Sven Egenhoff<sup>1</sup>

<sup>1</sup>University of North Dakota, Grand Forks, North Dakota, USA | <sup>2</sup>Oil Field Geomechanics, Richmond, Texas, USA | <sup>3</sup>Earth Science Department, Kent State University, Kent, Ohio, USA

**Correspondence:** Ghoulem Ifrene ([ghoulem.ifrene@und.edu](mailto:ghoulem.ifrene@und.edu))

**Received:** 5 March 2025 | **Revised:** 18 May 2025 | **Accepted:** 19 May 2025

**Funding:** This work was supported by North Dakota Industrial Commission.

**Keywords:** 3D printing | anisotropy | mechanical properties | stereolithography

## ABSTRACT

Stereolithography (SLA) 3D printing offers unprecedented opportunities for creating tailored materials with complex geometries. This study quantifies the impact of layer thickness and orientation on the mechanical and acoustic properties of SLA-printed materials under triaxial stress conditions, a critical yet understudied area. We fabricated models with layer dip angles of 0°, 45°, and 90°, and layer thicknesses of 25, 100, and 160 μm. These samples underwent triaxial compression testing and ultrasonic elastic wave velocity measurements using an Autolab 1500 triaxial load frame. Our findings reveal significant anisotropy in the mechanical properties of the 3D-printed samples, with up to a 30% increase in uniaxial compressive strength for 45° oriented samples. Additionally, we uncover a novel relationship between layer parameters and acoustic properties, enabling nondestructive quality assessment of 3D-printed components. This research provides a comprehensive framework for enhancing the performance of 3D-printed materials in high-stress applications, with critical insights into the behavior of SLA-printed materials under complex stress states, useful for aerospace, geomechanics, and biomedical engineering applications.

## 1 | Introduction

Three-dimensional (3D) printing technology, also known as advanced manufacturing (AM), is a rapidly developing field that has revolutionized manufacturing processes across various industries including aerospace [1], automotive [2, 3], healthcare [4], petroleum engineering [5–8], geomechanics [9–11], and architecture [12, 13]. This technology uses computer-aided design (CAD) to create three-dimensional objects by adding material layer by layer using almost any material such as polymers, ceramics, and thermal plastic urethane. Metals can also be employed as a raw material [14].

There are several techniques involved in 3D printing, including fused deposition modeling (FDM), stereolithography (SLA), selective laser sintering (SLS), digital light processing (DLP),

binder jetting, and material jetting. Each technique has its advantages and disadvantages, and the choice of technique depends on the type of object being printed, the desired resolution, and the available materials [15]. With the increasing popularity and availability of 3D printing technology, it is now easier than ever to create custom objects, prototypes, and even entire structures using 3D printing.

Among the available 3D printing techniques, SLA produces high-resolution objects with smooth surfaces. SLA was first developed in the early 1980s by Hideo [16]. The SLA printing process works by selectively curing photoreactive polymers with a laser [17]. The process begins with a 3D CAD model with a standard tessellation language (STL) file that is uploaded to the SLA printer. The printer then slices the model into thin layers and begins by first printing the bottom layer on a build platform in

## Summary

- Reduced layer thickness enhances stiffness and uniaxial compressive strength.
- $0^\circ$  print orientation maximizes pseudo-static Young's modulus under triaxial load.
- Increased layer thickness improves acoustic wave velocity but reduces unconfined compressive strength (UCS).

the X-Y plane (Figure 1) and then by adding support structures that are automatically detected and created for models based on the overhang angle. The build platform is submerged in a liquid resin sensitive to UV light. A laser then scans the bottom layer, selectively curing the resin where the model requires material. The build platform is then lifted by one layer in the Z axis, and the process is repeated until the entire object is printed. Once the printing is complete, the object is removed from the build platform and rinsed in a reagent (isopropyl alcohol) to remove any uncured resin. The object is then cured under UV light and heat to fully harden the resin into a finished product [18]. The resulting object has a high level of detail and accuracy, with smooth surfaces and precise dimensions [19]. SLA printing is commonly used in industries such as engineering, product design, and jewelry making, where high resolution and accuracy are required.

One of the important mechanical properties of 3D printed objects is their anisotropy [20, 21], which refers to the directional dependence of the physical properties of a material. In the case of SLA 3D printing, the objects produced can exhibit anisotropic behavior due to the specific printing process [22]. The anisotropy in SLA-printed objects results from the layer-by-layer printing process, which creates a specific orientation of the cured resin layers [22]. The orientation of these layers influences the mechanical properties of the printed objects, with some directions having higher strength and stiffness [23]. Furthermore, the degree of anisotropy in SLA-printed objects can also depend on specific printing parameters, such as the resin type, layer thickness, printing angle, and laser wattage [24, 25]. As a result, it is important to consider the

anisotropic properties of SLA-printed objects when designing and using them for specific applications, particularly where the mechanical behavior of the printed sample is important. This can involve optimizing the printing parameters and the orientation of the objects to achieve the desired mechanical properties. Some recent studies performed on AM materials to study the mechanical properties under various states of stress are shown in Table 1.

In this study, the influence of layer orientation and thickness on the mechanical and acoustic properties under compression was investigated by conducting confining and triaxial compression tests, along with acoustic compressional and shear wave velocity measurements. Notably, unlike most studies that have focused on the effects of printing layers and angles under tensile stress and uniaxial stress [34–37], this research shifts the focus to the behavior of 3D-printed materials under confining stress (triaxial). This distinction is important, as many engineering applications involve triaxial stresses, and understanding the material properties in such conditions is critical.

Our experimental data analysis investigates the impact of different layer thicknesses and orientations on the strength and stiffness of 3D-printed cylindrical specimens under triaxial stress. The results of this study contribute to the development of 3D printing technology and provide insights into the design and optimization of 3D-printed components for a range of applications including aerospace, geomechanics, and biomedical engineering.

## 2 | Methodology

This study employed a multi-faceted experimental approach to comprehensively characterize the mechanical and acoustic properties of 3D-printed samples. The core of our investigation involved three distinct, yet complementary, testing procedures: (1) ultrasonic velocity measurements, (2) triaxial compression testing, and (3) unconfined uniaxial compression testing. These tests were strategically designed to provide a holistic understanding of the material's behavior under varying stress conditions, ranging from static to dynamic, and under both confined and unconfined states.

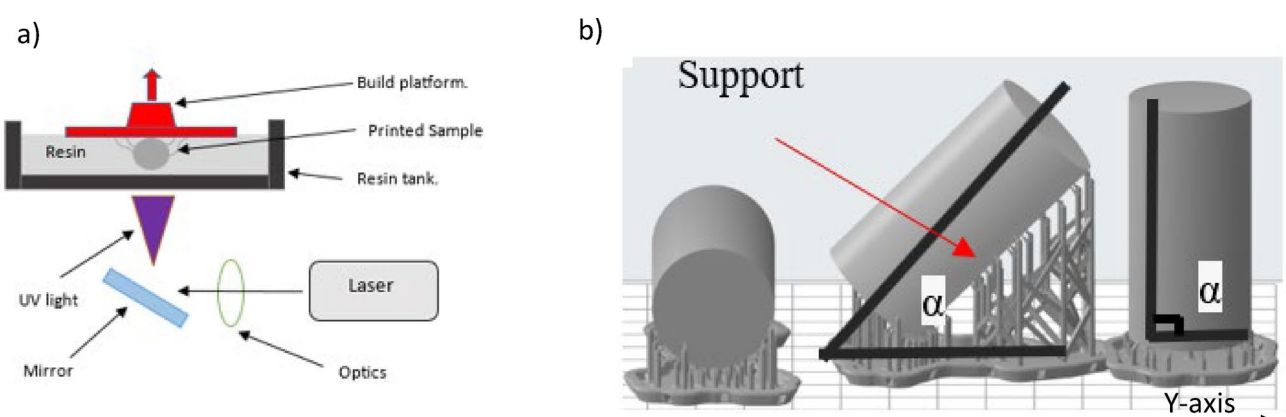


**FIGURE 1** | Illustration of the SLA 3D printing process and specimen build orientation (a) the stereolithography 3D printing process schematic. (b) View of the specimen's placing orientation during the process of 3D printing (CAD).

**TABLE 1** | Summary of literature on the use of 3D printing in geomechanics.

Application	Experiments	Used printing technology	References
Rock mechanics	Uniaxial compressive strength and tensile test	Fused deposition modeling (FDM)	[26]
Fracture mechanics	Uniaxial compressive strength and shearing experiments	Fused deposition modeling (FDM)	[9]
Fracture flow	Fluid flow experiments in single rough fracture	Stereolithography (SLA)	[27]
Fracture flow and rock mechanics coupling	Single rough fracture under stress (isotropic confinement)	Acrylonitrile butadiene styrene (ABS)	[28]
Marine structural applications	Triaxial compressive tests	3D printed PE fiber-reinforced concrete	[29]
Soft robotics	Uniaxial tests	Multi-material additive manufacturing	[30]
Biomedical	Uniaxial tests	Polylactic acid (PLA)	[31]
N/A	Tensile test flexural test	Fused deposition modeling (FDM)	[32]
N/A	Tensile tests	Stereolithography (SLA)	[18]
N/A	Tensile tests	Acrylonitrile styrene scrylate (ASA), polycarbonate ABS and ULTEM-9085	[33]

## 2.1 | 3D-Printed Specimen Fabrication

The Formlabs Form 3B+ printer, tailored for professional environments such as healthcare, engineering, and manufacturing, was employed in the production of the samples. The printed samples were fabricated using V4 gray polylactic acid (PLA) resin. In operation, the SLA printer features a reservoir containing liquid resin and a descending platform. As the platform reaches a specific depth, a laser beam is directed onto the resin, shaping the initial layer of the object (Figure 1). The laser initiates a chemical reaction within the resin, resulting in the formation of monomer chains that solidify and fuse with the preceding layer, ensuring structural integrity.

Subsequent to the completion of each layer, the build platform undergoes a small vertical displacement, and the process repeats for the next layer. This incremental layering continues until the entire (cylindrical, in this case) sample is fabricated.

To achieve specimens with varied transverse printing planes, the samples were fabricated at different angles ( $\alpha$ ), including  $0^\circ$ ,  $45^\circ$ , and  $90^\circ$ , as depicted in Figure 1. This approach enables the creation of specimens with differing printing orientations, thereby facilitating an exploration of the mechanical characteristics as a function of printing orientation. The printing angle ( $\alpha$ ) represents the angle between the principal axis of the specimen and the Y-axis of the printing platform, providing a means to precisely control the orientation of the printed objects for desired properties and behaviors.

To investigate the effect of layer thickness, 3D-printed samples with varying layer thicknesses were also created. Layer thickness is a key factor in the printing process, as it can impact the quality and strength of the final product. By adjusting the layer thickness, it is possible to achieve different levels of detail and

precision in the printed object. For example, thicker layers can be used to print objects more quickly, but with less detail, while thinner layers can produce more intricate designs but take longer to print. Additionally, varying the layer thickness can affect the strength and durability of the printed object. By experimenting with different layer thicknesses, it is possible to find the optimal setting for a specific printing project, and achieve the desired level of detail and strength. Three-layer thicknesses were adopted for this work. Samples at  $25$ ,  $100$ , and  $160\text{ }\mu\text{m}$  were printed using PreForm slicing software that can automatically slice, detect, and generate support structures for the models.

Upon completion of the printing process, the specimen was extracted from the printer and subjected to a solvent bath (98% isopropyl alcohol) to eliminate any excess resin. Subsequently, the object underwent curing under UV light at a temperature of  $60^\circ\text{C}$  for 1 h, ensuring the resin's complete hardening and durability (Figure 2). The dimensions of each specimen were measured both before and after the curing process. The shrinkage observed in the PLA samples ranged between 0.2% and 0.3%, which is considered negligible for triaxial testing.

## 2.2 | Laboratory Testing Setup and Procedures

The high-pressure/temperature, fully servo-controlled triaxial load frame, the AutoLab 1500 shown in Figure 3, at the University of North Dakota was employed. This system was designed and provided by New England Research Inc. This facility enables the execution of elastic and mechanical experiments, as depicted in the accompanying figure. The AutoLab 1500 system is designed to operate within two distinct pressure ranges, allowing for experimentation up to either 69 MPa (10,000 psi) or 138 MPa (20,000 psi), and can withstand



**FIGURE 2** | 3D SLA printed cylindrical specimens before washing and curing (left), and samples after washing and curing (right).

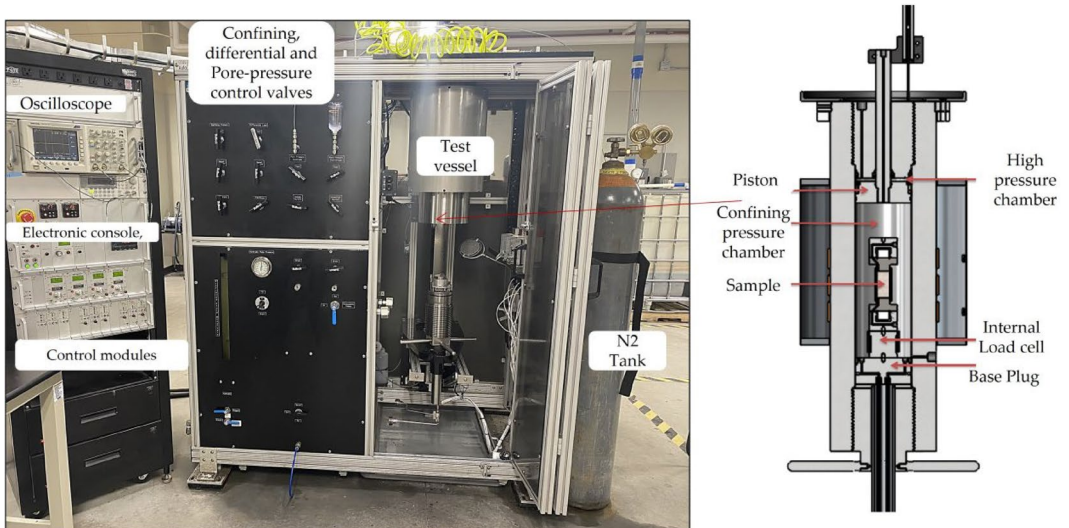


**FIGURE 3** | AutoLab 1500 instrument. The schematic diagram of the core holder and hydraulic system in the equipment (Autolab-1500) [38].

temperatures of up to 120°C (248°F). The experimental setup is adaptable to various combinations of confining pressures, pore pressure, and temperature conditions. It supports the execution of traditional rock mechanics testing techniques, such as isotropic (hydrostatic) compression, uniaxial compression, triaxial compression, viscoelastic deformation under stress-controlled loading rates, and strain-controlled loading rates; ultrasonic waveform measurements (including compressional and shear waves); and steady-state and pulse-decay permeability measurements. In total, nine specimens were prepared, with one specimen used per test to ensure consistency. Following the International Society for Rock Mechanics (ISRM) guidelines and utilizing the same setup employed during ultrasonic wave velocity measurements, axial and radial stresses and deformations were recorded using linear variable differential transducers (LVDTs).

### 2.3 | Correlated Experimental Design: A Holistic Approach

The testing program was designed to correlate the results from different tests and give a more complete understanding of the material's behavior. All experiments were conducted under controlled and consistent temperature conditions, with the temperature 29°C maintained constant by the AutoLab 1500 system across all tests and sample types. Table 2 shows the confining and differential stresses applied during the experiments.

#### 2.3.1 | Ultrasonic Velocity Measurements

During the sonic wave measurements, data were acquired by transmitting a compressional wave (P-wave) and two

perpendicular shear waves (S-wave) through the cylindrical samples. The set up utilized ultrasonic endcaps with a native frequency of 750 MHz and housing a piezoelectric crystal stack to generate the P-wave and two orthogonally polarized S-waves, denoted as S1 and S2. The sample was affixed to the source ultrasonic transducer velocity assembly with a shear wave couplant, while the receiver ultrasonic transducer velocity assembly was linked to the sample. The entire arrangement, inclusive of the specimen, was housed within a pressure vessel.

To initiate the data acquisition process, AutoLab's Linux-based software was used. Confining pressure was applied to the sample using mineral oil within the pressure vessel. Throughout the experiment, clear waveform acquisition was achieved by fine-tuning servo-controllers, adjusting the pressure chamber, advancing the axial piston, and configuring the oscilloscope settings too. Data were captured at various levels of confining pressure and, along with the ultrasonic velocity measurements, provided a baseline to which the testing results could be compared and interpreted.

**TABLE 2** | Table shows the confining and differential pressures applied during the experiments.

Experiments	Confining pressures	Differential stresses
Ultrasonic velocity measurements	1, 2, 4, 6, 8, 10, 15, and 20 MPa	0 MPa
Triaxial testing	1, 2, 4, 6, 8, 10, 15, and 20 MPa	3 MPa at each confining pressure
Unconfined compressive strength	1 MPa	Until the sample reached yield strength

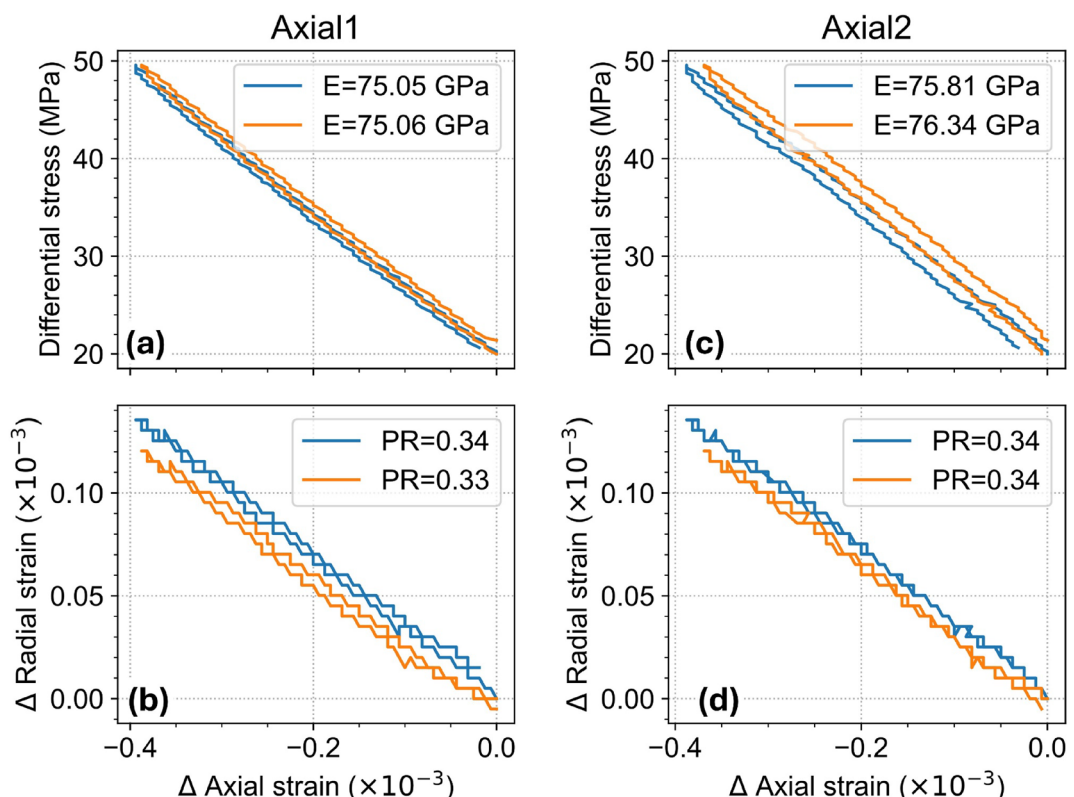


**FIGURE 4** | Mechanical response of aluminum samples under uniaxial loading, shown for two axial measurement channels (Axial1 and Axial2). (a, c) Differential stress versus axial strain for Axial1 and Axial2 configurations, respectively. (b, d) Corresponding radial strain plotted against axial strain, used to estimate Poisson's ratio (PR). The blue and orange curves correspond to two repeated loading-unloading tests.

### 2.3.2 | Triaxial Testing

Axial deformations and stress measurements under ambient conditions were calibrated using a known aluminum sample mechanical property (Figure 4).

The aluminum test results show an average Poisson's ratio of 0.33 and 75.56 GPa for Young's modulus, which are consistent with values reported in the literature [39–42].

The testing procedure involved a loading rate of 0.05 MPa/s. LVDTs were deployed to monitor axial and radial displacements, from which strains were calculated. Positioned approximately one radius above the upper end of the specimen, two LVDTs monitored axial displacement within a ring (Figure 5). The LVDTs were mounted on extended rods attached to a second ring, which was positioned approximately one specimen radius below the lower end.

Samples were subjected to different confining pressures; subsequently, axial stress was increased to 3 MPa and then reduced back to the initial confining pressure to observe both loading and

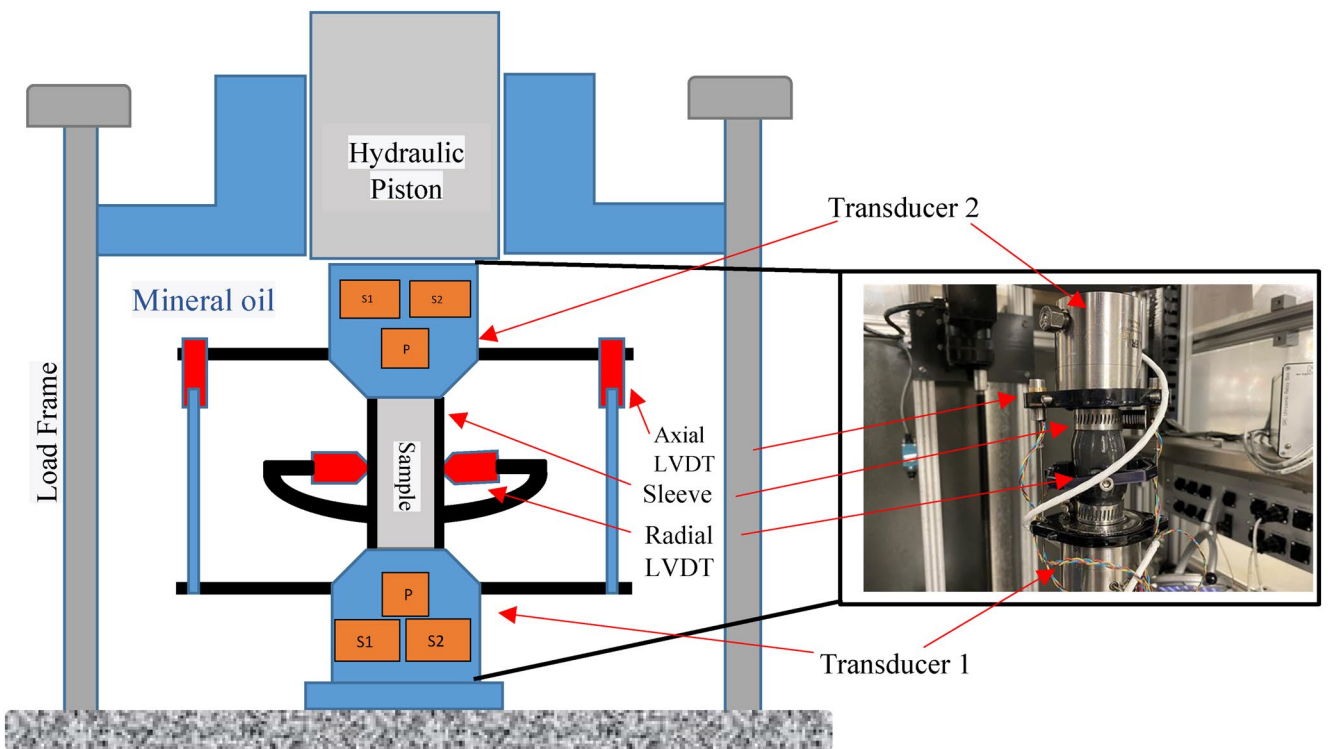


**FIGURE 5** | Illustration depicting the components housed within the pressure vessel of a servo-hydraulically controlled triaxial testing system; right: Sample assembly.

unloading responses. The pseudo-static Young's modulus (PSYM) and the effective Poisson's ratio representing the material's stiffness and lateral deformation response under confining pressure are then calculated at each level of confining pressure applied during the triaxial experiment.

### 2.3.3 | Unconfined Compression Testing

This test was conducted to determine the unconfined compressive strength (UCS) of the 3D-printed samples. The samples were loaded until failure (the following convention is used: compressive stress is positive).

After completing ultrasonic and triaxial testing, both the axial and confining pressures were reduced to the minimal level of the AutoLab frame (1 MPa). Following this, axial loading at a rate of 0.006 mm/s was initiated. Concurrently, axial and radial deformations alongside axial stress were recorded. The tests continued until the axial stress reached a plateau, indicating no further increments in stress. The 3D-printed specimens did not display a stress drop after reaching their ultimate yield strength. Instead, they exhibited a gradual stress increase, eventually reaching an asymptotic value. This asymptotic limit was defined as the ultimate strength of the sample.

## 3 | Results

### 3.1 | Unconfined Compression Tests

After conducting UCS tests on the cylindrical 3D printed samples, noticeable, bulging, and buckling were observed in the samples (Figure 6). The presence of bulging suggested lateral



**FIGURE 6** | Left: Sample before testing. Right: Sample after testing.

expansion of the samples under compressive loading and was indicative of plastic deformation within the material. Additionally, buckling, characterized by sudden lateral deflection or bending, was evident in some samples and indicated a loss of structural integrity under the applied compressive stress.

The observed bulging led to Poisson's ratios exceeding 0.5 for all samples. The high Poisson's ratio arose from outward expansion along the circumference of the samples under axial loading due to the lattice structure of the 3D printed samples [43].

In the investigation of the ultimate UCS of the 3D printed samples, nine printing configurations were assessed with differing layer thicknesses and print angles (Table 3). The UCS data revealed a discernible trend where samples with a layer thickness

**TABLE 3** | Samples characteristics.

Sample	1	2	3	4	5	6	7	8	9
Layer thickness ( $\mu\text{m}$ )	25	25	25	100	100	100	160	160	160
Layer angle (degrees)	0	45	90	0	45	90	0	45	90
Density ( $\text{Kg/m}^3$ )	1176	1177	1176	1174	1167	1165	1166	1159	1159
UCS (MPa)	67	58.8	67	57.1	55.2	53.2	57.8	58.6	50

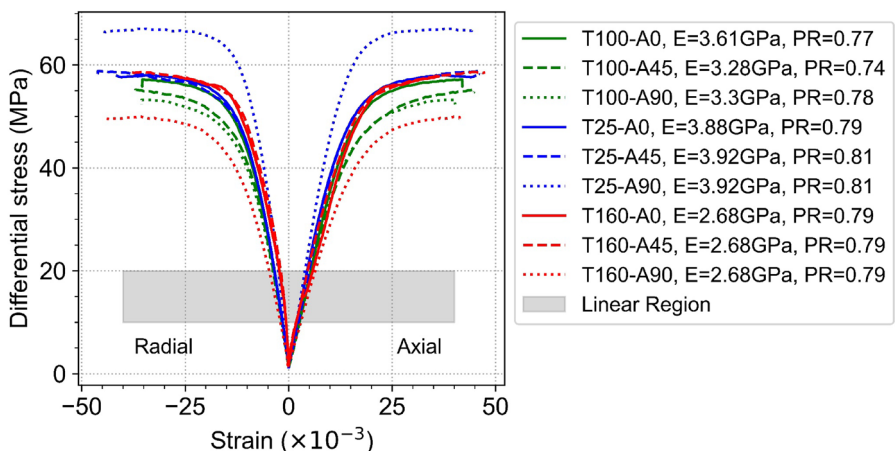


**FIGURE 7** | Axial and radial stress–strain response under unconfined conditions for samples of different thicknesses ( $T = 25 \mu\text{m}$ ,  $T = 100 \mu\text{m}$ ,  $T = 160 \mu\text{m}$ ) and three angles ( $A = 0^\circ$ ,  $A = 45^\circ$ ,  $A = 90^\circ$ ). Sample labels follow the format  $\text{TXX-AYY}$ , where  $T$  denotes thickness and  $A$  denotes angle. Each curve shows both axial and radial strain evolution with differential stress. The shaded gray band highlights the linear stress–strain region used to compute Young's modulus (E) and Poisson's ratio (PR). Legend entries include corresponding E and PR values derived from linear fits in this region.

of  $25 \mu\text{m}$ , irrespective of the print angle, consistently exhibited the highest UCS values, peaking at  $67 \text{ MPa}$ , suggesting that at this layer thickness, the angle of deposition had less impact on the UCS of the sample (Figure 7). As layer thickness was increased to  $100 \mu\text{m}$  and beyond, a decrement in UCS was observed, with the  $160 \mu\text{m}$ ,  $90^\circ$  angle sample demonstrating the lowest UCS at  $50 \text{ MPa}$ . Samples printed with a  $45^\circ$  angle presented an intermediate UCS across all layer thickness categories, implying that this angle may provide a balance between structural integrity and the material's mechanical properties. Furthermore, a slight decrease in density (measured by water displacement method), with increasing layer thickness and a printing angle deviating from  $0^\circ$ , was noted, which may contribute to the variations in UCS. The data clearly indicated that layer thickness is perhaps the most important factor in determining the UCS of 3D printed materials using the SLA technique, and that optimizing the print angle can potentially enhance the mechanical performance of the samples.

The  $25 \mu\text{m}$  samples exhibited the highest stiffness with Young's modulus values at or above  $3.88 \text{ GPa}$ . This suggests that at finer layer thicknesses, the printed material tends to be stiffer and more resistant to elastic deformation. As the layer thickness was increased to  $100 \mu\text{m}$ , there was a noticeable decrease in stiffness, with Young's modulus values dropping to a range between  $3.28$  to  $3.61 \text{ GPa}$ . This drop indicates that thicker layers may not bond as tightly or may have larger defects, resulting in a less rigid structure. The  $160 \mu\text{m}$  samples had the lowest Young's modulus values, all at  $2.68 \text{ GPa}$ , which was consistent across all printing angles.

This uniform reduction in stiffness might be due to inherent properties of the material when printed at this specific layer thickness, such as increased porosity or less effective layer adhesion.

For the  $25 \mu\text{m}$  thickness samples, Young's modulus was higher at  $45^\circ$  and  $90^\circ$  ( $3.92 \text{ GPa}$ ) compared to  $0^\circ$  ( $3.88 \text{ GPa}$ ). This slight increase suggests that, at this layer thickness, an angled deposition may contribute marginally to stiffness. In the  $100 \mu\text{m}$  thickness samples, there was a notable decrease in Young's modulus with an increase in the printing angle from  $0^\circ$  ( $3.61 \text{ GPa}$ ) to  $45^\circ$  ( $3.28 \text{ GPa}$ ) and a slight increase at  $90^\circ$  ( $3.3 \text{ GPa}$ ). This indicates that at this thickness, the material's stiffness is influenced more significantly by the print angle, with  $45^\circ$  resulting in the least stiff material. For the  $160 \mu\text{m}$  samples, Young's modulus remained consistent across all angles ( $2.68 \text{ GPa}$ ), indicating that at this greater thickness, the effect of printing angle on stiffness is negligible. This could be due to the fact that at larger layer thicknesses, the influence of interlayer bonding and potential voids between layers overshadows the effects of print orientation.

The Poisson's ratios for the  $25$ - and  $160 \mu\text{m}$  thicknesses were predominantly higher, especially at  $45^\circ$  and  $90^\circ$  angles, with values peaking at  $0.81$ . This could suggest that these configurations, despite their differences in stiffness, may undergo similar volumetric changes when under stress. The  $100 \mu\text{m}$  thickness samples showed more variation in Poisson's ratio, ranging from  $0.74$  to  $0.78$ . The lower Poisson's ratio at the  $45^\circ$  angle could indicate less lateral deformation, which might be due to an optimal orientation of the print layers that balances deformation characteristics.

The test results indicate that Poisson's ratio values do not vary significantly with the change in layer angle for the same layer thickness, implying that the angle of deposition has a minimal impact on this specific property.

### 3.2 | PSYM and Effective Poisson's Ratio

Figures 8, A1, and A2 display triaxial test results for various combinations of layer thicknesses and angles.

PSYM showed significant variation with printing orientation. Figure 9a details (PSYM) of 3D printed samples at various printing orientations ( $0^\circ$ ,  $45^\circ$ , and  $90^\circ$ ) and layer thicknesses (25, 100, and  $160\mu\text{m}$ ), several key observations can be made regarding the mechanical behavior of these materials under different confining pressures during both loading and unloading cycles. It is evident that the printing orientation significantly affects the pseudo-static modulus. The  $0^\circ$  orientation typically exhibits higher modulus values across most confining pressures compared to the  $45^\circ$  and  $90^\circ$  orientations. This suggests that samples printed with layers aligned along the load direction ( $0^\circ$ ) are stiffer, possibly due to better load transfer along continuous layers. The samples with a smaller layer thickness ( $25\mu\text{m}$ ) generally show higher moduli than those with thicker layers (100 and  $160\mu\text{m}$ ). This trend could be attributed to a more compact structure with fewer defects in finer layers, leading to an enhanced ability to bear load.

The modulus for all samples increases with an increase in confining pressure up to a certain point, beyond which the growth rate of modulus either plateaus or declines. This trend suggests

that while confining pressure helps in compacting the material and enhancing load-bearing capacity initially, there is a threshold beyond which additional pressure does not contribute significantly to modulus enhancement or could even lead to structural weaknesses.

The loading curves are generally higher than the unloading curves, indicating hysteresis (more accentuated for the  $45^\circ$  samples) in the mechanical response. This hysteresis could be due to energy dissipation through mechanisms like micro-cracking or plastic deformation that occurs during the first loading.

Effective Poisson's ratio for 3D printed samples was analyzed under different conditions of printing orientation ( $0^\circ$ ,  $45^\circ$ ,  $90^\circ$ ) and layer thickness (25, 100,  $160\mu\text{m}$ ). The data are presented for both the loading and unloading phases, as well as averaged values, across a range of confining pressures from 2.5 to 20 MPa (Figure 9b).

The samples printed at a  $0^\circ$  orientation typically exhibit a higher effective Poisson's ratio compared to those printed at  $45^\circ$  and  $90^\circ$ . This trend points toward an anisotropy associated with the printing direction, which significantly influences the mechanical behavior of the samples under triaxial stress. Among the different layer thicknesses, the  $25\mu\text{m}$  samples show the lowest Poisson's ratio. This could imply that finer layers yield a denser or more uniform structure, which limits lateral deformation under compressive loads. Conversely, the  $160\mu\text{m}$  samples demonstrate a notable difference in Poisson's ratio between the loading and unloading phases, suggesting that thicker layers may be prone to more significant structural inhomogeneities, which could affect their mechanical reliability.

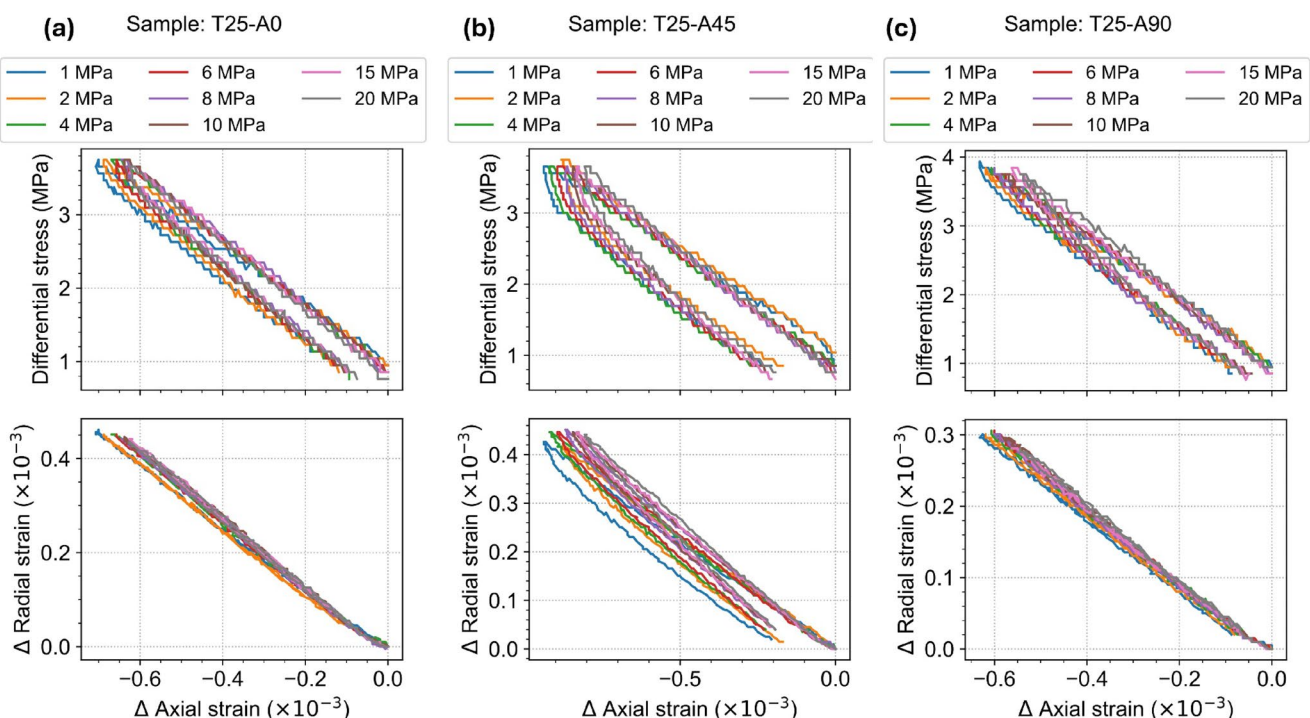


**FIGURE 8** | Axial and radial strain response during triaxial loading of samples with 25 mm thickness at three layer orientations: (a) T25-A0 ( $0^\circ$ ), (b) T25-A45 ( $45^\circ$ ), and (c) T25-A90 ( $90^\circ$ ). Each plot displays differential stress versus  $\Delta$  axial strain (top row) and  $\Delta$  radial strain versus  $\Delta$  axial strain (bottom row) across a range of confining pressures from 1 to 20 MPa.

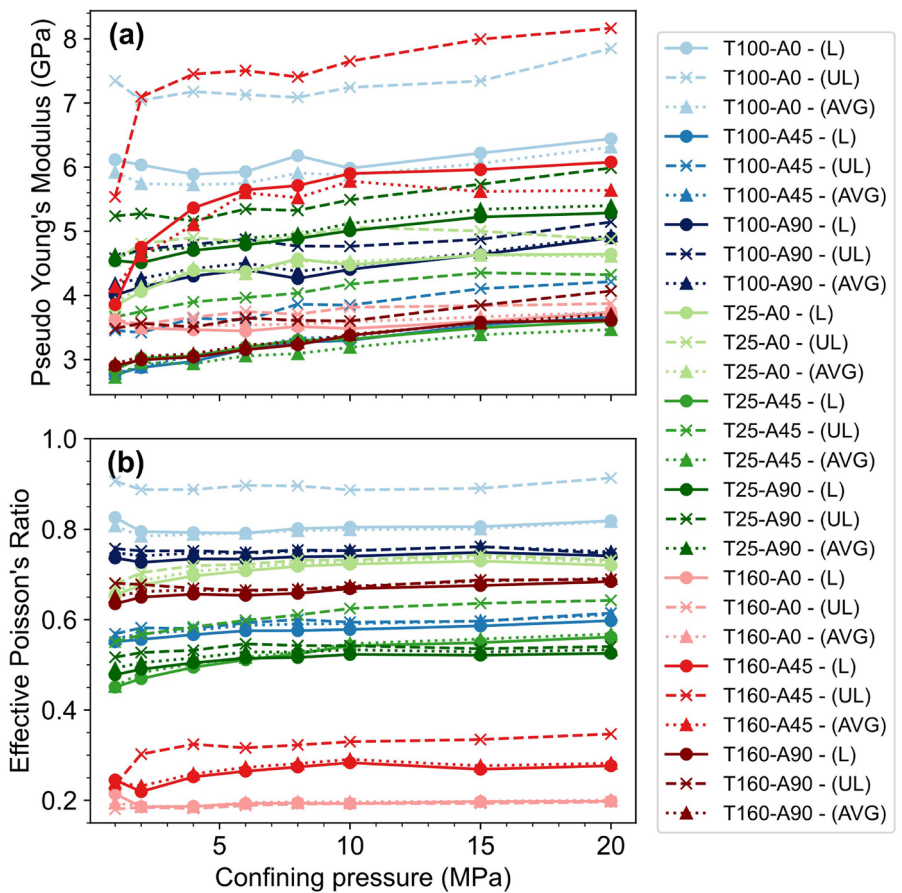


**FIGURE 9** | Variation of (a) Pseudo Young's modulus and (b) effective Poisson's ratio with confining pressure for samples of different thicknesses ( $T = 25 \mu\text{m}$ ,  $T = 100 \mu\text{m}$ ,  $T = 160 \mu\text{m}$ ) and three angles ( $A = 0^\circ$ ,  $A = 45^\circ$ ,  $A = 90^\circ$ ). For each sample, modulus is estimated from the linear portion of loading (L), unloading (UL), and the average of both (AVG) branches. Sample labels follow the format TXX-AYY, where T denotes thickness and A denotes angle. Modulus values are computed from axial stress-strain response during triaxial loading.

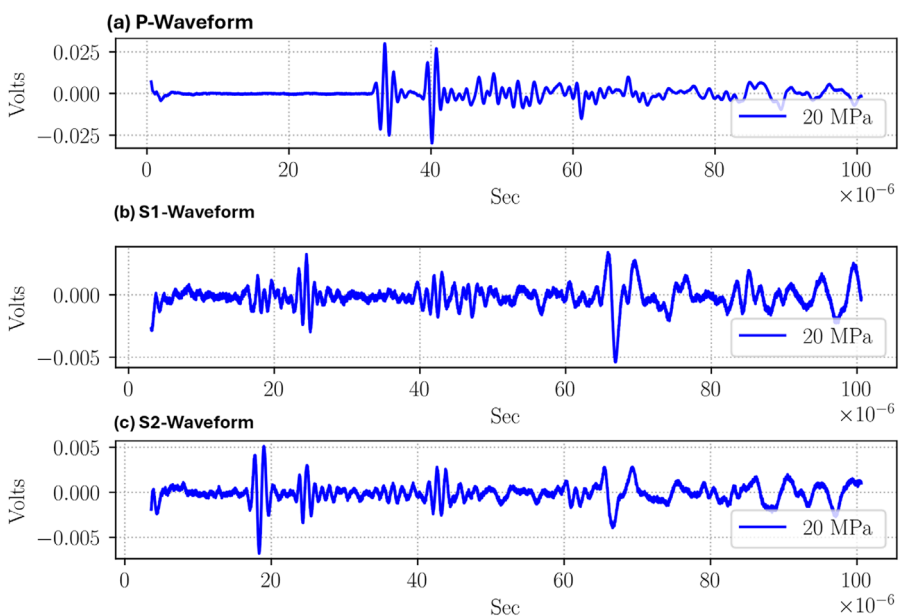


**FIGURE 10** | Ultrasonic waveforms recorded for sample T25-A0 at 20 MPa confining pressure. (a) P-wave, (b) first shear wave (S1), and (c) second shear wave (S2). Each trace shows voltage as a function of time over a 100  $\mu\text{s}$  window. T25-A0 refers to a specimen with 25  $\mu\text{m}$  thickness and  $0^\circ$  orientation.

During loading, a consistently higher effective Poisson's ratio is observed across most sample types when compared to the unloading phase. This difference suggests potential energy dissipation mechanisms within the material, such as microstructural rearrangements or irreversible damage.

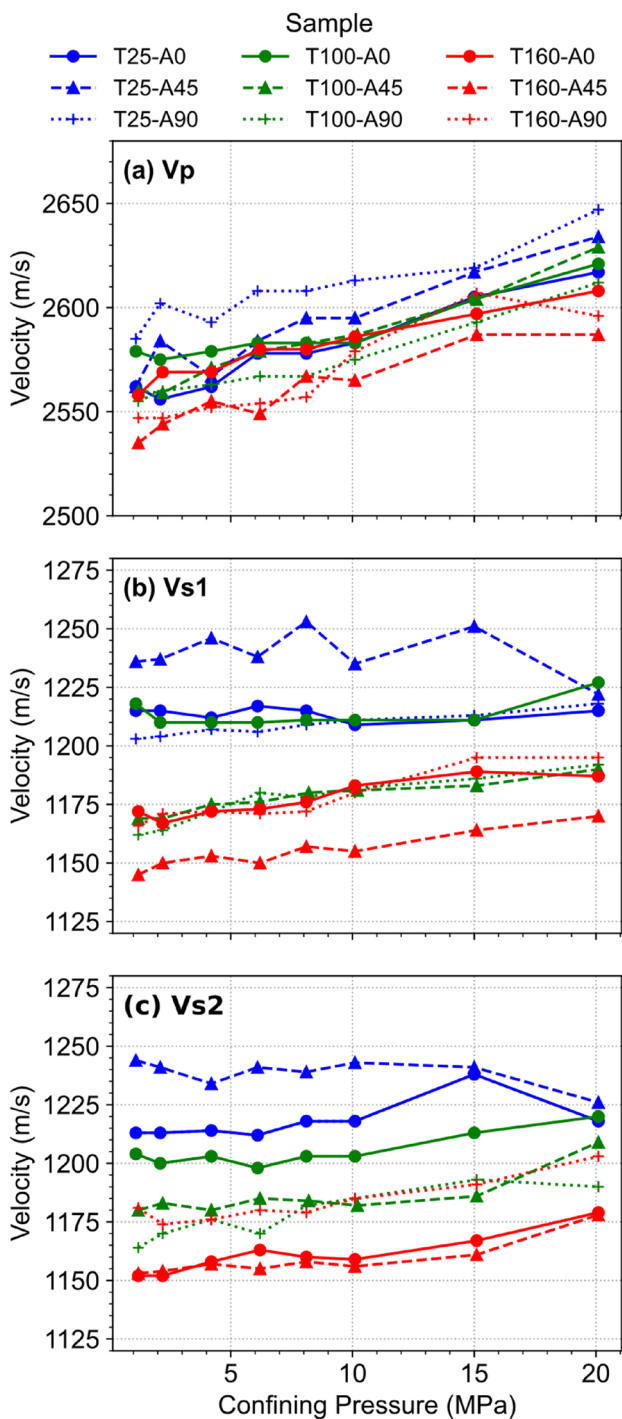


**FIGURE 11 |** Compressional and shear wave velocities plotted against confining pressure for samples with three thicknesses ( $T=25\text{ }\mu\text{m}$ ,  $T=100\text{ }\mu\text{m}$ ,  $T=160\text{ }\mu\text{m}$ ) and three angles ( $A=0^\circ$ ,  $A=45^\circ$ ,  $A=90^\circ$ ). Sample labels follow the format TXX-AYY, where  $T$  indicates thickness ( $\mu\text{m}$ ) and  $A$  indicates printing angle (degrees). (a) Compressional wave velocity ( $V_p$ ), (b) and (c) two orthogonal shear wave velocities ( $V_{s1}$ ) and ( $V_{s2}$ ).

The data underscore the substantial impact of both microstructural characteristics (like printing orientation and layer thickness) and macroscopic stress conditions (such as confining pressure) on the mechanical properties of 3D printed materials.

### 3.3 | Acoustic Results

P wave and shear waves (S1 and S2) were recorded in real-time as they traversed the 3D-printed specimens during triaxial testing. Figure 10 illustrates the progression of P-wave and S-waves (S1 and S2) propagation throughout the entire triaxial process in a representative sample. Additional examples from other specimens are provided in the Figures A3, A4, and A5.

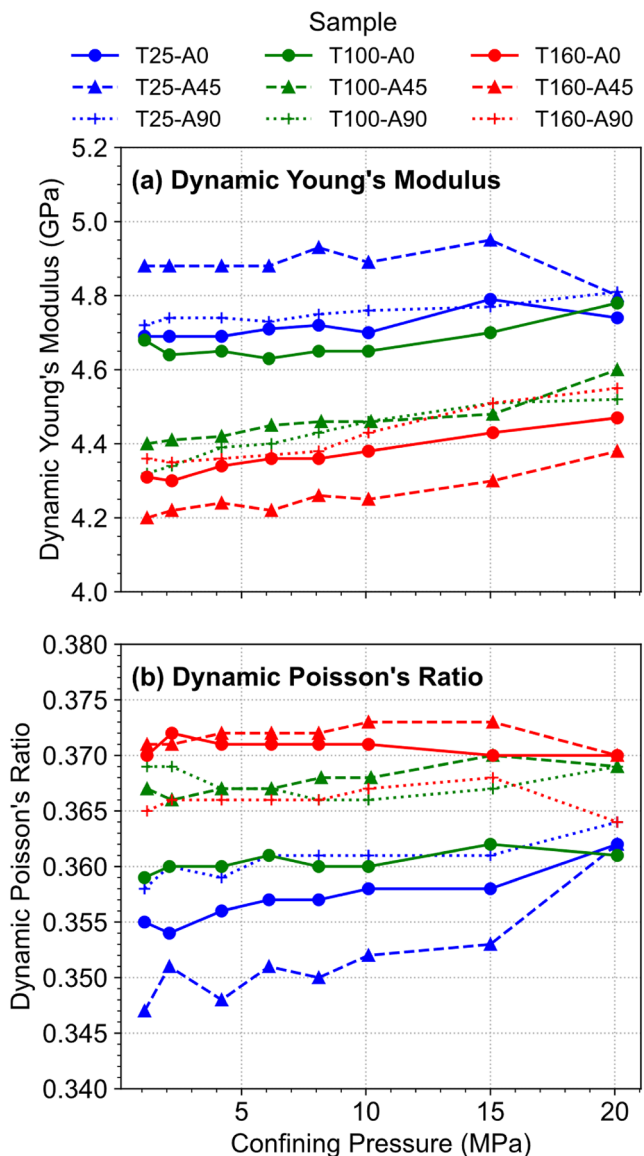


**FIGURE 12 |** Dynamic elastic properties as a function of confining pressure for samples with different thicknesses ( $T=25\text{ }\mu\text{m}$ ,  $T=100\text{ }\mu\text{m}$ ,  $T=160\text{ }\mu\text{m}$ ) and three angles ( $A=0^\circ$ ,  $A=45^\circ$ ,  $A=90^\circ$ ). Sample labels follow the format TXX-AYY, where  $T$  indicates thickness ( $\mu\text{m}$ ) and  $A$  indicates printing angle (degrees). (a) Dynamic Young's modulus, (b) dynamic Poisson's ratio.

The acoustic data revealed that the compressional wave velocity ( $P$ ) tended to increase with layer thickness. Specifically, samples with a thickness of  $160\text{ }\mu\text{m}$  consistently exhibited higher  $P$  values compared to those with  $25\text{ }\mu\text{m}$ , suggesting that a thicker layer structure enhances the material's ability to propagate sound waves due to increased stiffness. However, the orientation of the layers ( $0^\circ, 45^\circ, 90^\circ$ ) showed minimal influence on  $P$ , indicating isotropic behavior in compressional wave propagation across the tested range (Figure 11a).

Shear wave velocities ( $S_1$  and  $S_2$ ) displayed slight variances with layer orientation (Figure 11b,c), particularly noting anisotropy between the two orthogonal directions measured. This effect was more pronounced at a  $45^\circ$  layering angle, which may be attributed to the internal layer alignment offering different resistance to shear stress. Similarly, the shear wave velocities were generally higher in samples with a  $160\text{ }\mu\text{m}$  thickness, aligning with the trends observed in compressional wave velocity, and pointing to a universally stiffer matrix at this layer thickness.

Dynamic Young's modulus increased with layer thickness across all samples (Figure 12a). The highest modulus was observed in the  $160\text{ }\mu\text{m}$  samples, reinforcing the correlation between layer thickness and material stiffness. This parameter peaked at the  $45^\circ$  angle for several sets, suggesting that this particular orientation might optimize alignment of the layers to better resist dynamic stresses.

Dynamic Poisson's ratio across different samples was relatively consistent, with minor fluctuations suggesting that changes in layer thickness and angle did not significantly affect the material's dynamic characteristic to deform laterally under longitudinal stress (Figure 12b). This uniformity in Poisson's Ratio under varying structural conditions illustrates the material's stable deformation response to external stresses.

## 4 | Conclusions

This study provides a comprehensive investigation into the mechanical and acoustic properties of SLA-printed materials under triaxial stress conditions, addressing a critical gap in the existing literature. Our findings demonstrate the significant influence of layer thickness and orientation on the anisotropic behavior of these materials.

Specifically, we observed that finer layers ( $25\text{ }\mu\text{m}$ ) exhibited higher stiffness, strength, and uniformity compared to thicker layers ( $160\text{ }\mu\text{m}$ ). Conversely, thicker layers exhibit higher compressional and shear wave velocities, suggesting an enhanced ability to propagate sound waves due to increased structural stiffness. Particular layer orientations, particularly around  $45^\circ$ , can lead to improvements in compressive strength, with up to a 30% increase observed. Anisotropic behavior was evident in the shear wave velocities and PSYM, with samples printed at a  $0^\circ$  orientation consistently exhibiting superior stiffness and strength.

Dynamic and effective Poisson's ratios exhibited consistent trends across varying layer thicknesses and orientations, indicating stable lateral deformation characteristics under stress.

The acoustic analysis further corroborated the mechanical findings, emphasizing the influence of layer thickness on wave propagation properties. The uniformity in dynamic Poisson's ratio across samples suggests that SLA-printed materials maintain a predictable deformation response, which is critical for applications in engineering, aerospace, and biomedical fields.

These results complement the conventional focus on tensile and uniaxial testing, highlighting the importance of considering triaxial stress states for a more accurate representation of material behavior in real-world engineering applications. Our findings provide a framework for optimizing printing parameters to achieve desired mechanical properties, enabling the design and fabrication of more reliable and efficient 3D-printed structures.

Future research should focus on expanding the scope of this study by exploring a wider range of materials, printing techniques, and stress conditions. Additionally, the development of advanced simulation models that incorporate the observed anisotropic behavior is crucial for predicting the performance of 3D-printed components in complex loading scenarios. By building upon the foundation laid by this research, we can unlock the full potential of 3D printing technology and revolutionize the way we design and manufacture materials for a diverse range of applications.

## Author Contributions

G.I. contributed to the experimental setup, performed data collection, and prepared the original draft. K.S. performed critical review and co-prepared the original draft. N.N. supported the validation and formal analysis and assisted in drafting technical sections. P.P. contributed to the literature review, figure preparation, and experimental setup. R.S. performed critical review of the manuscript. S.E. supervised the project and secured funding.

## Acknowledgments

We would like to express our sincere gratitude to Dr. Marisela Nagel and Nikolas Bittner for their guidance and support throughout this research. Additionally, we extend our deepest appreciation to the North Dakota Industrial Commission (NDIC), whose generous financial support was instrumental in making this study possible.

## Data Availability Statement

Data will be made available on request.

## References

- C. Richter and H. Lipson, "Untethered Hovering Flapping Flight of a 3D-Printed Mechanical Insect," *Artificial Life* 17, no. 2 (2011): 73–86.
- M. Gebler, A. J. M. S. Uiterkamp, and C. Visser, "A Global Sustainability Perspective on 3D Printing Technologies," *Energy Policy* 74 (2014): 158–167.
- S. L. Rahim and S. Maidin, "Feasibility Study of Additive Manufacturing Technology Implementation in Malaysian Automotive Industry Using Analytic Hierarchy Process," *Advanced Materials Research* 903 (2014): 450–454.
- H. Dodziuk, "Applications of 3D Printing in Healthcare," *Polish Journal of Cardio-Thoracic Surgery* 13, no. 3 (2016): 283–293.

5. L. Kong, S. Ishutov, F. Hasiuk, and C. Xu, "3D Printing for Experiments in Petrophysics, Rock Physics, and Rock Mechanics: A Review," *SPE Reservoir Evaluation and Engineering* 24, no. 4 (2021): 721–732.
6. S. Ishutov, T. D. Jobe, S. Zhang, et al., "Three-Dimensional Printing for Geoscience: Fundamental Research, Education, and Applications for the Petroleum Industry," *American Association of Petroleum Geologists Bulletin* 102, no. 1 (2018): 1–26.
7. E. M. Kataoka, R. C. Murer, J. M. Santos, et al., "Simple, Expendable, 3D-Printed Microfluidic Systems for Sample Preparation of Petroleum," *Analytical Chemistry* 89, no. 6 (2017): 3460–3467.
8. A. G. Almetwally and H. Jabbari, "3D-Printing Replication of Porous Media for Lab-Scale Characterization Research," *ACS Omega* 6, no. 4 (2021): 2655–2664.
9. Q. Jiang, X. Feng, L. Song, Y. Gong, H. Zheng, and J. Cui, "Modeling Rock Specimens Through 3D Printing: Tentative Experiments and Prospects," *Acta Mechanica Sinica* 32 (2016): 101–111.
10. L. Kong, M. Ostadhassan, S. Zamiran, B. Liu, C. Li, and G. G. Marino, "Geomechanical Upscaling Methods: Comparison and Verification via 3D Printing," *Energies* 12, no. 3 (2019): 382.
11. L. Song, Q. Jiang, Y. E. Shi, et al., "Feasibility Investigation of 3D Printing Technology for Geotechnical Physical Models: Study of Tunnels," *Rock Mechanics and Rock Engineering* 51 (2018): 2617–2637.
12. R. Mathur, "3D Printing in Architecture," *International Journal of Innovative Science, Engineering and Technology* 3, no. 7 (2016): 583–591.
13. K. Zhang, Y. R. Liu, M. H. Xiao, J. T. Chen, and Q. Yang, "Study on Fractured Rock-Like Materials for Geomechanical Model Test Based on 3D Printing Technology," *IOP Conference Series: Earth and Environmental Science* 861. IOP Publishing (2021): 22031.
14. N. Shahrubudin, T. C. Lee, and R. Ramlan, "An Overview on 3D Printing Technology: Technological, Materials, and Applications," *Procedia Manufacturing* 35 (2019): 1286–1296.
15. A. Jandyal, I. Chaturvedi, I. Wazir, A. Raina, and M. I. U. Haq, "3D Printing—A Review of Processes, Materials and Applications in Industry 4.0," *Sustainable Operations and Computers* 3 (2022): 33–42.
16. H. Kodama, "Automatic Method for Fabricating a Three-Dimensional Plastic Model With Photo-Hardening Polymer," *Review of Scientific Instruments* 52, no. 11 (1981): 1770–1773.
17. T. Finnes, "High Definition 3d Printing—Comparing Sla and Fdm Printing Technologies," *Journal of Undergraduate Research* 13, no. 1 (2015): 3.
18. F. Cosmi and A. Dal Maso, "A Mechanical Characterization of SLA 3D-Printed Specimens for Low-Budget Applications," *Materials Today Proceedings* 32 (2020): 194–201.
19. X. L. Ma, "Research on Application of SLA Technology in the 3D Printing Technology," *Applied Mechanics and Materials* 401 (2013): 938–941.
20. S. Aravind Shanmugam, J. Razmi, M. J. Mian, and L. Ladani, "Mechanical Anisotropy and Surface Roughness in Additively Manufactured Parts Fabricated by Stereolithography (SLA) Using Statistical Analysis," *Materials* 13, no. 11 (2020): 2496.
21. R. Zou, Y. Xia, S. Liu, et al., "Isotropic and Anisotropic Elasticity and Yielding of 3D Printed Material," *Composites Part B: Engineering* 99 (2016): 506–513.
22. J. Stögerer, S. Baumgartner, T. Rath, and J. Stampfl, "Analysis of the Mechanical Anisotropy of Stereolithographic 3D Printed Polymer Composites," *European Journal of Materials* 2, no. 1 (2022): 12–32.
23. N. Zohdi and R. Yang, "Material Anisotropy in Additively Manufactured Polymers and Polymer Composites: A Review," *Polymers* 13, no. 19 (2021): 3368.
24. T. Yao, Z. Deng, K. Zhang, and S. Li, "A Method to Predict the Ultimate Tensile Strength of 3D Printing Polylactic Acid (PLA) Materials With Different Printing Orientations," *Composites Part B: Engineering* 163 (2019): 393–402.
25. A. Husna, S. Ashrafi, A. N. M. A. Tomal, N. T. Tuli, and A. B. Rashid, "Recent Advancements in Stereolithography (SLA) and Their Optimization of Process Parameters for Sustainable Manufacturing," *Hybrid Advances* 7 (2024): 100307.
26. C. Jiang and G. F. Zhao, "A Preliminary Study of 3D Printing on Rock Mechanics," *Rock Mechanics and Rock Engineering* 48 (2015): 1041–1050.
27. P. Yin, C. Zhao, J. Ma, C. Yan, and L. Huang, "Experimental Study of Non-Linear Fluid Flow Through Rough Fracture Based on Fractal Theory and 3D Printing Technique," *International Journal of Rock Mechanics and Mining Sciences* 129 (2020): 104293.
28. T. Phillips, T. Bultreys, K. Bisdom, et al., "A Systematic Investigation Into the Control of Roughness on the Flow Properties of 3D-Printed Fractures," *Water Resources Research* 57, no. 4 (2021): 25233.
29. J. J. Zeng, X. Hu, H. Q. Sun, Y. Liu, W. J. Chen, and Y. Zhuge, "Triaxial Compressive Behavior of 3D Printed PE Fiber-Reinforced Ultra-High Performance Concrete," *Cement and Concrete Composites* 155 (2025): 105816.
30. S. Janbaz, F. S. L. Bobbert, M. J. Mirzaali, and A. A. Zadpoor, "Ultra-Programmable Buckling-Driven Soft Cellular Mechanisms," *Materials Horizons* 6, no. 6 (2019): 1138–1147.
31. H. Bakhtiari, A. Nouri, and M. Tolouei-Rad, "Impact of 3D Printing Parameters on Static and Fatigue Properties of Polylactic Acid (PLA) Bone Scaffolds," *International Journal of Fatigue* 186 (2024): 108420.
32. S. K. Dhinesh, P. S. Arun, K. K. L. Senthil, and A. Megalingam, "Study on Flexural and Tensile Behavior of PLA, ABS and PLA-ABS Materials," *Materials Today Proceedings* 45 (2021): 1175–1180.
33. V. R. Viswanath, S. Hiremath, and D. S. Chiniwar, "Using Extrusion-Based 3D Printing Technology to Investigate the Impact of Changing Print Conditions on Tensile Characteristics," *Rapid Prototyping Journal* 30, no. 5 (2024): 987–999.
34. J. W. Frascati, "Effects of Position, Orientation, and Infiltrating Material on Three Dimensional Printing Models," 2007.
35. M. Dawoud, I. Taha, and S. J. Ebeid, "Mechanical Behaviour of ABS: An Experimental Study Using FDM and Injection Moulding Techniques," *Journal of Manufacturing Processes* 21 (2016): 39–45.
36. C. W. Ziemian, D. E. Cipoletti, S. N. Ziemian, M. N. Okwara, and K. V. Haile, "Monotonic and Cyclic Tensile Properties of ABS Components Fabricated by Additive Manufacturing," 2014.
37. O. S. Es-Said, J. Foyos, R. Noorani, M. Mendelson, R. Marloth, and B. A. Pregger, "Effect of Layer Orientation on Mechanical Properties of Rapid Prototyped Samples," *Materials and Manufacturing Processes* 15, no. 1 (2000): 107–122.
38. P. Pothana, G. Ifrene, and K. Ling, "Stress-Dependent Petrophysical Properties of the Bakken Unconventional Petroleum System: Insights From Elastic Wave Velocities and Permeability Measurements," *Fuel* 4, no. 4 (2023): 397–416.
39. "The Engineering ToolBox," accessed March 30, 2025, <https://www.engineeringtoolbox.com/>.
40. J. F. Labuz, S. T. Dai, and E. Papamichos, "Plane-Strain Compression of Rock-Like Materials," in *International Journal of Rock Mechanics and Mining Sciences & Geomechanics Abstracts*, vol. 33 (Elsevier, 1996), 573–584.
41. Y. Lv, J. Liu, and Z. Xiong, "One-Dimensional Dynamic Compressive Behavior of Dry Calcareous Sand at High Strain Rates," *Journal*

of Rock Mechanics and Geotechnical Engineering 11, no. 1 (2019): 192–201.

42. M. J. Mehl, “Pressure Dependence of the Elastic Moduli in Aluminum-Rich Al-Li Compounds,” *Physical Review B* 47, no. 5 (1993): 2493–2500.

43. X. Xue, C. Lin, F. Wu, Z. Li, and J. Liao, “Lattice Structures With Negative Poisson’s Ratio: A Review,” *Materials Today Communications* 34 (2023): 105132.

### Supporting Information

Additional supporting information can be found online in the Supporting Information section.